

# SaNet: Scale-aware Neural Network for Semantic Labelling of Multiple Spatial Resolution Aerial Images

Libo Wang<sup>1</sup>, Shenghui Fang<sup>1\*</sup>, Ce Zhang<sup>2,3</sup>, Rui Li<sup>1</sup>, Chenxi Duan<sup>4</sup>, Xiaoliang Meng<sup>1</sup>, Peter M. Atkinson<sup>2,5,6</sup>

1. School of Remote Sensing and Information Engineering, Wuhan University, Wuhan 430079, China.

2. Lancaster Environment Centre, Lancaster University, LA1 4YQ, U.K.

3. UK Centre for Ecology & Hydrology, Lancaster, LA1 4AP, U.K.

4. The State Key Laboratory of Information Engineering in Surveying, Mapping, and Remote Sensing, Wuhan University, Wuhan 430079, China.

5. Geography and Environmental Science, University of Southampton, Highfield, Southampton SO17 1BJ, UK.

6. Institute of Geographic Sciences and Natural Resources Research, Chinese Academy of Sciences, 11A Datun Road, Beijing 100101, China.

**KEYWORDS:** Aerial Image, Deep Neural Network, Multiple Spatial Resolution, Scale-aware Feature, Semantic Segmentation.

## ABSTRACT:

Assigning geospatial objects of aerial images with specific categories at the pixel level is a fundamental task in urban scene interpretation. Along with rapid developments in sensor technologies, aerial images can be captured at multiple spatial resolutions (MSR) with information content manifested at different scales. Extracting information from these MSR aerial images represents huge opportunities for enhanced feature representation and characterisation. However, MSR images suffer from two critical issues: 1) increased variation in the sizes of geospatial objects and 2) information and informative feature loss at coarse spatial resolutions. In this paper, we propose a novel scale-aware neural network (SaNet) for semantic labelling of MSR aerial images to address these two issues. SaNet deploys a densely connected feature network (DCFPN) module to capture high-quality multi-scale context, such as to address the scale variation issue and increase the quality of segmentation for both large and small objects simultaneously. A spatial feature recalibration (SFR) module is further incorporated into the network to learn complete semantic features with enhanced spatial relationships, where the effects of information and informative feature loss are addressed. The combination of DCFPN and SFR allows the proposed SaNet to learn scale-aware features from MSR aerial images. Extensive experiments undertaken on ISPRS semantic segmentation datasets demonstrated the outstanding accuracy of the proposed SaNet in cross-resolution segmentation, with an average OA of 83.4% on the Vaihingen dataset and an average F1 score of 80.4% on the Potsdam dataset, outperforming state-of-the-art deep learning approaches, including FPN (80.2% and 76.6%), PSPNet (79.8% and 76.2%) and Deeplabv3+ (80.8% and 76.1%) as well as DDCM-Net (81.7% and 77.6%) and EaNet (81.5% and 78.3%).

## 1. INTRODUCTION

Spatial resolution plays a crucial role in Earth Observation tasks (Atkinson and Tate, 2000; Ge et al., 2019), especially for the semantic segmentation of aerial images, involving dense pixel-level classification. Such semantic segmentation is applied widely for urban scene understanding (e.g. building and road extraction; Griffiths and Boehm, 2019; Wei et al., 2017), land cover classification (Zhang et al., 2018b, 2019) and change detection (Zhao et al., 2018a). Benefitting from rapid developments in sensor technology, aerial images are captured increasingly at multiple spatial resolutions (MSR). Thus, research on the semantic segmentation of aerial images is shifting towards cross-resolution segmentation to leverage the available multi-scale information jointly (Zheng et al., 2020b).

In recent years, deep convolutional neural networks (DCNNs) have brought significant advantages to a range of applications, with their hierarchical feature representation and high-level object characterization. Such advantages have been demonstrated clearly compared with traditional machine learning methods, such as support vector machine (SVMs) (Guo et al., 2018), random forests (RF) (Pal, 2005), and conditional random fields (CRFs) (Zhong and Wang, 2007). Influenced by the wave of DCNNs, semantic labelling of very fine resolution (VFR) aerial images has advanced greatly (Audebert et al., 2018; Zhang et al., 2018a). However, with cross-resolution segmentation of aerial images, there are two underlying issues: 1) MSR aerial images can reveal scale-dependent variation within and between geospatial objects that presents both opportunities and challenges for segmentation and 2) the semantic context captured is incomplete at coarse spatial resolutions due to information and feature loss. As illustrated in **Fig. 1**, cross-resolution segmentation of aerial images is an extremely challenging task.

The scale variation issue in MSR aerial images often results in biased segmentation of large and small objects. Multi-scale representation has great potential to solve this and related problems (Zhang et al., 2020; Zhao and Du, 2016). Several methods have been proposed to increase the multi-scale representation of deep networks (Li et al., 2021a; Li et al., 2021b). The image pyramid method was first developed to enhance multi-scale representation at the image level, which feeds MSR images into the network and fuses the prediction results at multiple scales. However, such an image pyramid method involves time-consuming training and inference processes, which are undesirable for pixel-based semantic segmentation tasks (Chen et al., 2016). Thereafter, the pyramidal feature hierarchy (PFH) method was proposed for efficient multi-scale representation, where a multi-scale structure with multi-layer feature maps was contrasted to capture the inherent multi-scale information (Cai et al., 2016; Singh and Davis, 2018). Further, the feature pyramid network (FPN) was designed by adding an extra top-down pathway to integrate low-level detailed features and high-level semantic features (Lin et al., 2017). The FPN-based methods, such as PANet (Liu et al.), NAS-FPN (Ghiasi et al., 2019), and BiFPN (Tan et al., 2020), are capable of capturing generalised semantic information compared with PFH methods. Recently, the spatial pyramid pooling (SPP) architecture was developed to enhance multi-scale representation by enlarging the receptive fields of semantic features. Typical SPP architectures include PSPNet (Zhao et al., 2017) and the Deeplab series (Chen et al., 2017; Chen et al., 2018a;

Chen et al., 2018b). However, existing multi-scale methods demonstrate limited quality and fidelity for segmenting MSR aerial images, partly due to information and informative feature loss at coarse spatial resolutions.

To address the loss of information and informative features in coarse spatial resolution aerial images, spatial feature recalibration is proposed which recalibrates semantic features with enhanced spatial relationships to capture intact and powerful context information (Jaderberg et al., 2015). The spatial relationship between geospatial objects should be invariant when the spatial resolution coarsens. Thus, strengthening spatial relationships could greatly benefit the feature representation of MSR aerial images. Previous research has focused on introducing spatial relationships into image segmentation networks for spatial feature recalibration. Liu et al. (2017) enhanced spatial relationships by learning local linear spatial propagation, resulting in high-quality semantic segmentation. Pan et al. (2018) proposed a spatial convolutional neural network with slice-by-slice convolutions to strengthen the spatial relationship by emphasizing informative features, which achieved a high accuracy of image segmentation. Mou et al. (2020) deployed a single-branched spatial relationship module into the fully convolutional network (FCN) (Long et al., 2015) to model long-range spatial dependencies, which enhanced the segmentation performance on VFR aerial images.

Different from these existing approaches, we address the scale variation issue and the informative feature loss issue jointly in the same network for semantic segmentation of MSR aerial images. Specifically, we propose a scale-aware neural network (SaNet) with two novel modules, including a densely connected feature pyramid network (DCFPN) module and a spatial feature recalibration (SFR) module, to extract scale-aware features for increasing the quality of segmentation from MSR aerial images. The DCFPN module combines the advantages of SPP-based and FPN-based methods in multi-scale representations by densely connecting multi-layer features and large field features. In particular, DCFPN employs a weighted fusion (WF) operation to fuse features instead of adding them directly which strengthens the multi-scale representation and balances the segmentation quality between large and small objects. The SFR module constructs two branches of different sizes designed for enhancing the spatial relationship of the network, which is capable of learning the intact context of geospatial objects, so as to tackle the informative feature loss issue in MSR aerial images. The structure of our SaNet is elegantly designed and separable into two modules (DCFPN and SFR), which are also easily transplanted into other DCNNs to be trained end-to-end automatically. The major contributions of this paper are, thus, summarized as follows:

- (1) A novel scale-aware neural network (SaNet) is proposed for semantic segmentation of multi-scale geospatial objects in MSR aerial images.
- (2) The proposed DCFPN module captures high-quality multi-scale context by a weighted fusion of multi-layer features and large field features and, therefore, classifies multi-scale geospatial objects unbiasedly from MSR aerial images.
- (3) The proposed SFR module is built with a dual-branched structure to enhance the spatial relationship of high-level semantic features, which increases the adaptability of the model to MSR aerial images.

The remainder of this paper is organized as follows. Related work is reviewed briefly in Section 2. The architecture of SaNet and its components are detailed in Section 3. Ablation studies on two datasets, the ISPRS Vaihingen dataset and the Potsdam dataset, together with a comprehensive comparison between SaNet and a set of benchmarks are provided in Section 4. Finally, conclusions are drawn in Section 5.

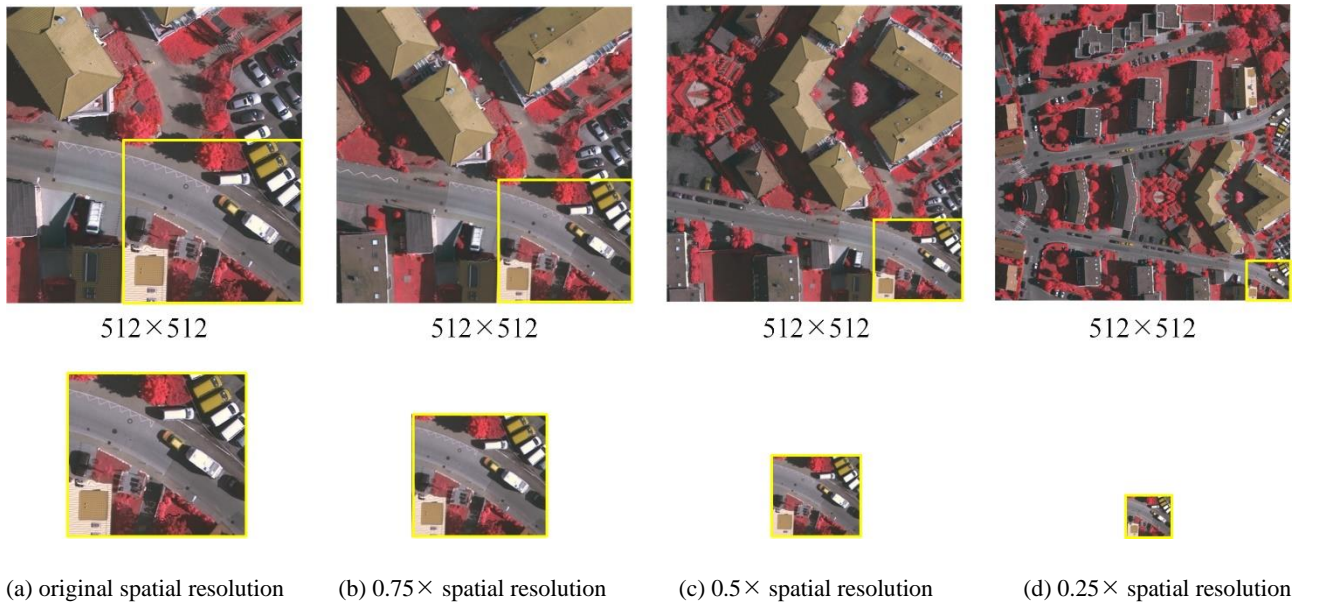


**Fig. 1** Illustration of the loss of information about geospatial objects in MSR aerial images at different spatial resolutions. Each image is a  $512 \times 512$  pixel patch. Variation in the sizes of geospatial objects has been enlarged in MSR aerial images, and information and informative features are lost as spatial resolution decreases, particularly the detailed information. As shown in the highlighted yellow region, the details of vehicles are clear at the original spatial resolution, but much reduced at  $0.25 \times$  spatial resolution.

## 2. RELATED WORK

### 2.1 Multi-scale representation for semantic segmentation

The problem of scale variation of geospatial objects exists commonly in the semantic segmentation of VFR aerial images, for example, making it difficult to balance feature extraction between large and small objects (Zheng et al., 2020a). Multi-scale representation methods have been studied to balance feature extraction across objects with different sizes, including the image pyramid, pyramidal feature hierarchy (PFH), feature pyramid network (FPN), and spatial pyramid pooling (SPP) architectures.

Image pyramid methods obtain a multi-scale representation by training parallel networks with input images at several resolutions (Chen et al., 2016; Singh and Davis, 2018; Zhao et al., 2018b). However, learning multi-scale features in such a fashion is inefficient due to the complicated training and hand-crafted input sizes. PFH methods utilize multi-layer feature maps with different sizes to encode the multi-scale information, which increases the efficiency of the model compared to image pyramid methods (Li et al., 2018; Roy et al., 2019). PFH, however, lacks robustness in feature extraction. To enhance the multi-scale representation robustly without increasing extensive computational complexity, FPN-based methods were investigated extensively in recent years. For example, the path aggregation network (PANet) adds an extra bottom-up path to enrich information flow (Liu et al.). The bi-directional feature pyramid network (BiFPN) repeatedly constructs cross-scale connections for weighted multi-layer feature fusion (Tan et al., 2020). Nevertheless, the fixed receptive field of extracted features restricts the representation capability of FPN-based methods. For receptive field enlargement, SPP-based methods employ dilated convolutions or parallel pooling layers of different sizes (Chen et al., 2017; Chen et al., 2018a; Chen et al., 2018b; Zhao et al., 2017). The dense dilated convolutions merging network (DDCM-Net) fuses densely linked dilated convolutions to capture robust multi-scale contexts (Liu et al., 2020), while the edge-aware neural network (EaNet) develops a large kernel pyramid pooling module to extract powerful large field features (Zheng et al., 2020a).

Scale variation is increasingly complex in MSR aerial images, where a single multi-scale representation is unable to meet the requirement of cross-resolution aerial image segmentation. We proposed the DCFPN module for high-quality multi-scale representation in MSR aerial images by combining the advantages of the fused multi-layer features in FPN and the large field features in SPP.

### 2.2 Spatial relationship modelling

Modelling spatial relationships using networks for high-quality semantic segmentation has attracted much attention in recent years (Bell et al., 2016; Hu et al., 2019; Santoro et al., 2017). Spatial propagation networks focus on neighbour information to model the local spatial relationship, which limits spatial representations (Cheng et al., 2018; Jaderberg et al., 2015; Liu et al., 2017). Recently, modelling global spatial relationships or long-range dependencies has become a new research direction for feature representation. Persello and Stein (2017) developed a deep FCN to capture long-range dependencies to increase levels of abstraction. Wang et al. (2018) presented a nonlocal block to capture long-range global spatial dependencies for spatial relationship enhancement and optimized the segmentation results. Xu et al. (2019) proposed a spatial-temporal relationship module to strengthen the compatibility of extracted features in terms of geometry and topology. Fu et al. (2019) appended an attention module on top of a dilated FCN to model the semantic interdependencies in the spatial dimension. Huang et al. (2020) built an Omni range dependencies network to capture comprehensive context information for spatially complex scene parsing. However, these spatial relationship networks were constructed using a single-branched structure with fixed sizes, restricting their representational ability in MSR aerial images.

In this research, we developed a spatial feature recalibration (SFR) module to enhance the global spatial relationship of our model for the cross-resolution aerial image segmentation task. The SFR module builds a dual-branched structure to model spatial relationships at different scales, which preserves the integrity of the extracted semantic features effectively to alleviate the influence of information loss at coarse spatial resolutions.

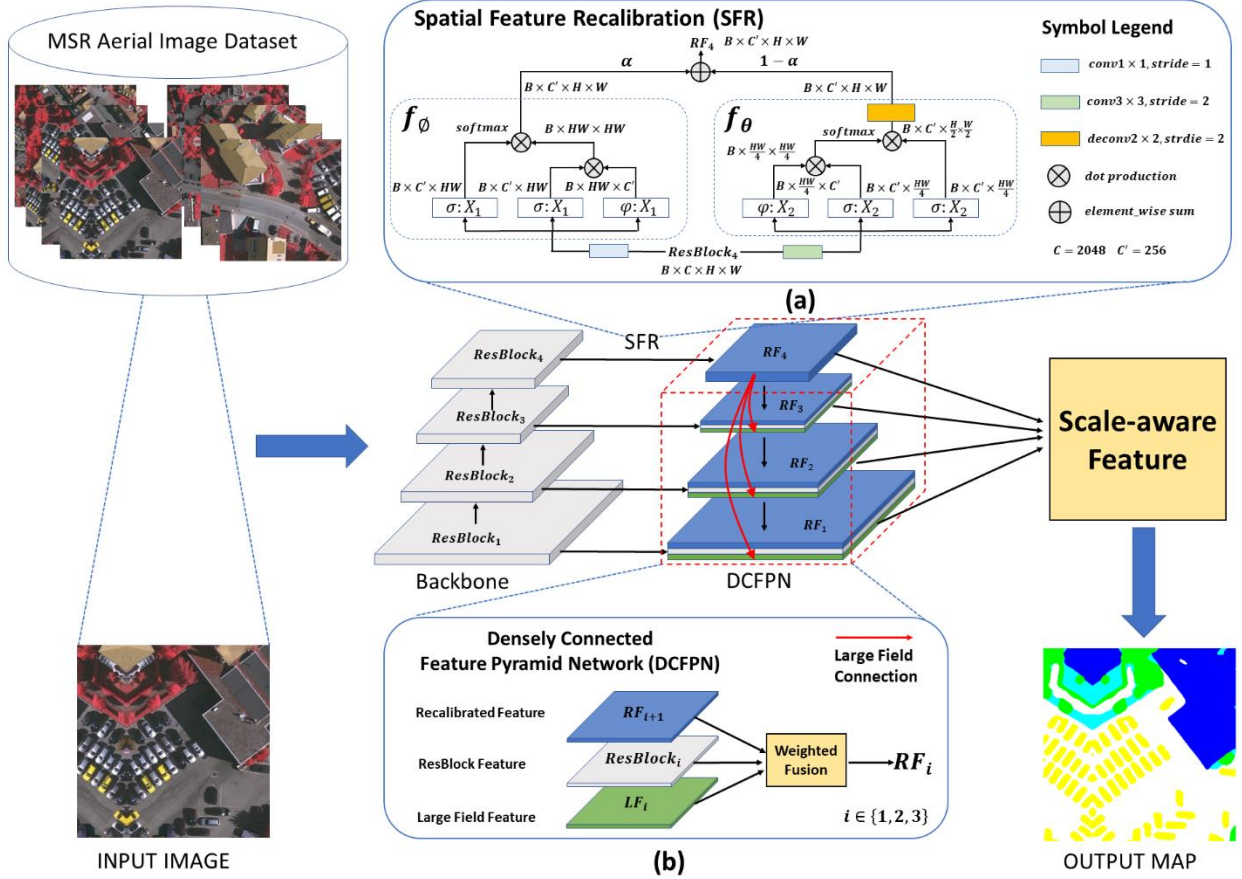


Fig. 2 The entire architecture of the proposed SaNet.

### 3. THE ARCHITECTURE OF THE PROPOSED SANET

The overall architecture of the proposed SaNet is composed of the ResNet backbone (He et al., 2016), SFR and DCFPN, as shown in Fig. 2. The ResNet backbone consists of four residual blocks, extracting the corresponding four ResBlock features from the input image:  $ResBlock_1$ ,  $ResBlock_2$ ,  $ResBlock_3$  and  $ResBlock_4$ . Especially,  $ResBlock_4$  is downscaled 16 times and its size is the same as  $ResBlock_3$ . Considering the efficiency of SaNet, SFR is deployed on top of the ResNet backbone to recalibrate the high-level semantic feature  $ResBlock_4$ . Thereafter, the recalibrated feature  $RF_4$  is fed into DCFPN. DCFPN employs three large field connections, marked by red arrows, to generate large field features from  $RF_4$ , and constructs a top-down pathway for fusing ResBlock features (grey), recalibrated features (blue) and large field features (green) adaptively. The three layers of DCFPN produce three recalibrated features with high-quality multi-scale contexts (i.e.,  $RF_1$ ,  $RF_2$  and  $RF_3$ ) which are then fused with  $RF_4$  to generate the scale-aware feature for final segmentation.

#### 3.1 Spatial relationship enhancement with SFR

To address the issue of information loss at coarse spatial resolutions, we design a spatial feature recalibration (SFR) module that can model invariant spatial relationships between geospatial objects, thereby increasing the feature representation ability of the network. Previously, Mou et al. (2020) and Wang et al. (2018) constructed a single-branch structure with a dot production operation for global spatial relationship modelling. Differently, SFR constructs two branches of different sizes to model the global spatial relationship at diverse scales, remedying the limitation of the single branch structure that can extract only the fixed-scale spatial interactions from MSR aerial images. As shown in Fig. 2 (a), the input is the high-level semantic feature  $ResBlock_4$  and the output is the recalibrated feature  $RF_4$ . By applying two convolution layers with different kernel sizes and strides, the input  $ResBlock_4$  is divided into two branch features,  $X_1$  and  $X_2$ . The generation process of  $X_1$  and  $X_2$  of can be formalized as follows:

$$X_1 = ResBlock_4 \cdot W_1[C, C', K_1, S_1] \quad (1)$$

$$X_2 = ResBlock_4 \cdot W_2[C, C', K_2, S_2] \quad (2)$$

where  $K_1 = 1$  and  $S_1 = 1$  represent the size and stride of the filter  $W_1$ . Similarly,  $K_2 = 3$  and  $S_2 = 2$  represent the size and stride of the filter  $W_2$ .  $C = 2048$  and  $C' = 256$  denote the input channels and output channels, respectively. Operated on by the two convolution layers, the size of  $X_1$  is twice the size of  $X_2$ .

The generated  $X_1$  and  $X_2$  are fed into the spatial functions  $f_\emptyset$  and  $f_\theta$ , respectively, to provide information on the global spatial relationship. Thereafter, the spatially enhanced features are merged by a weighted element-wise sum operation to generate  $RF_4$ :

$$RF_4(X_1, X_2) = \alpha \cdot f_\emptyset(X_1) + (1 - \alpha) \cdot f_\theta(X_2) \quad (3)$$

Here,  $\alpha$  is a trainable variable to suppress redundant features produced during the merging process. The spatial functions  $f_\emptyset$  and  $f_\theta$  can be defined as:

$$f_\emptyset(X_1) = \emptyset \left( \sigma(X_1) \cdot f_s(\varphi(X_1) \cdot \sigma(X_1)) \right) \quad (4)$$

$$f_\theta(X_2) = \theta \left( \sigma(X_2) \cdot f_s(\varphi(X_2) \cdot \sigma(X_2)) \right) \quad (5)$$

where  $f_s$  represents the softmax activation function. The detailed implementation steps of  $f_\emptyset$  and  $f_\theta$  are as follows:

- 1) The feature map  $X_1$  is reshaped by  $\sigma$  and  $\varphi$  into  $C' \times HW$  and  $HW \times C'$ , respectively. Similarly, the feature map  $X_2$  is reshaped into  $C' \times \frac{HW}{4}$  and  $\frac{HW}{4} \times C'$ .
- 2) A dot production operation is applied to  $\sigma(X_1)$  and  $\varphi(X_1)$  to produce the spatial relationship matrix  $HW \times HW$ , which is further fed into the softmax activation function  $f_s$  to generate the probability map for feature recalibration. Meanwhile,  $\sigma(X_2)$  and  $\varphi(X_2)$  are processed by a similar procedure, but the shape of the corresponding probability map is  $\frac{HW}{4} \times \frac{HW}{4}$ .
- 3) The probability map is multiplied by  $\sigma(X_1)$  to generate the spatial recalibrated feature of  $X_1$ . The spatial recalibrated feature of  $X_2$  is generated in the same way. Further, the operation  $\emptyset$  resizes the spatial recalibrated feature of  $X_1$  to  $C' \times H \times W$ , while the combined operation  $\theta$  deploys a deconvolution layer to upsample the spatial recalibrated feature of  $X_2$  and then resize it to  $C' \times H \times W$ .

Processed by the two branches, the recalibrated feature  $RF_4$  is abundant in information relating to the global spatial relationships and capable of capturing unbroken semantic content from coarse spatial resolutions aerial images.

### 3.2 High-quality multi-scale representation with DCFPN

We proposed a novel FPN module for balanced semantic segmentation of multi-scale ground objects within MSR aerial images. Since this novel module utilizes the large field connections to densely connect the feature pyramid network (FPN) (Lin et al., 2017), we name it densely connected feature pyramid network (DCFPN). The main advantage of DCFPN is to capture rich and high-quality multi-scale contexts through a weighted fusion of semantic features at different scales and receptive fields. The structure of DCFPN is illustrated in **Fig. 2**.

#### 3.2.1 Large field connection

As shown in the dashed red box region of **Fig. 2**, to match the structure of the ResNet backbone, we designed three large field connections in DCFPN. Each connection contains a 2-D dilated convolution (Chen et al., 2018b) to generate the corresponding large field feature ( $LF_i$ ) from the recalibrated feature  $RF_4$ , whereafter the stacked deconvolutions are adopted to control the output size when necessary. The large field connection is defined as a function with the following equation:

$$LF_i(RF_4) = T_{3-i} \circ D_i(RF_4), \quad i \in \{1, 2, 3\} \quad (6)$$

where  $i$  denotes the layer index.  $T^\circ$  is a resize function that performs a  $2 \times 2$  deconvolution with stride 2 repeatedly, and  $3 - i$  denotes the number of repetitions.  $D_i$  denotes a 2-D dilated convolution for receptive field enlargement, which can be defined as:

$$D_i(RF_4) = \sum_{k_1=1}^K \sum_{k_2=1}^K RF_4[m + f_r(i) \cdot k_1, n + f_r(i) \cdot k_2] \cdot w[k_1, k_2] \quad (7)$$

where  $[m, n]$  and  $[k_1, k_2]$  represent the spatial position indices of the output  $D_i$  and the convolution filter  $w$ , respectively. Here,  $K$  is set to 3.  $f_r(i)$  denotes the dilated rate of  $D_i$  which can be computed as follow:

$$f_r(i) = 24 - 6i \quad (8)$$

According to different layers, the large field connection can produce large field features with diverse receptive fields and sizes, enabling the network to provide richer multi-scale contexts for feature fusion.

#### 3.2.2 Weighted Fusion

The three generated large field features are fused with the corresponding ResBlock features and recalibrated features by a weighted element-wise sum operation, as exhibited in **Fig. 2 (b)**. The equation is as follows:

$$RF_i = \begin{cases} RF_i, & i = 4 \\ \alpha_1 \cdot f_\mu(RF_{i+1}) + \alpha_2 \cdot f_\delta(ResBlock_i) + \alpha_3 \cdot LF_i, & i \in \{1,2,3\} \end{cases} \quad (9)$$

where  $f_\mu$  is a resize operation to unify the shape of  $RF_{i+1}$  and  $LF_i$ , while  $f_\delta$  is a standard  $1 \times 1$  convolution to unify the channels of  $ResBlock_i$  and  $LF_i$ .  $\alpha_1, \alpha_2, \alpha_3$  denote the weight coefficients and always satisfy  $\alpha_1 + \alpha_2 + \alpha_3 = 1$ .

Eventually, to capitalise on the benefits provided by spatial relationship enhancement and high-quality multi-scale representation, we further merge  $RF_1, RF_2, RF_3, RF_4$  to generate the scale-aware feature ( $SF$ ) for final segmentation. The formula is as follows:

$$SF = RF_1 + RF_2 + RF_3 + RF_4 \quad (10)$$

## 4. EXPERIMENTAL RESULTS AND DISCUSSION

### 4.1 Experimental settings

#### 4.1.1 Dataset

**Vaihingen.** The Vaihingen dataset consists of 33 very fine spatial resolution true orthophoto (TOP) image tiles at an average size of  $2494 \times 2064$  pixels. Each TOP image tile has three multispectral bands (Near Infrared, Red, Green) as well as the digital surface model (DSM) and the normalized digital surface model (NDSM) with a 9 cm ground sampling distance (GSD). The dataset involves five foreground classes (impervious surface, building, low vegetation, tree, car) and one background class (clutter). Following the recommendation by Liu et al. (2020) and Mou et al. (2020), 16 image tiles were selected as the training set, and the remaining 17 image tiles as the test set. Note, only TOP image tiles were used in our experiments without DSM.

**Potsdam.** The Potsdam dataset contains 38 very fine resolution TOP image tiles (GSD 5cm) at a size of  $6000 \times 6000$  pixels and involves the same category information as the Vaihingen dataset. Four multispectral bands (Red, Green, Blue, and Near Infrared), as well as a DSM and NDSM, are provided in the dataset. The 24 image tiles were chosen as the training set, and the remaining tiles were selected as the test set. We utilized only TOP image tiles with three multispectral bands (Near Infrared, Red, Green) in the experiments.

#### 4.1.2 Evaluation Metrics

The performance of the proposed method was evaluated by the F1 score and overall accuracy (OA), which were calculated based on an accumulated confusion matrix:

$$precision = \frac{1}{k} \sum_{c=1}^k \frac{TP_c}{TP_c + FP_c}; \quad (11)$$

$$recall = \frac{1}{k} \sum_{c=1}^k \frac{TP_c}{TP_c + FN_c}; \quad (12)$$

$$F1 = 2 \times \frac{precision \times recall}{precision + recall}; \quad (13)$$

$$OA = \frac{\sum_{c=1}^k TP_c}{N} \quad (14)$$

where  $c$  represents the index of the five foreground classes,  $k = 5$  denotes the number of classes.  $TP_c, TN_c, FP_c$  and  $FN_c$  indicate samples of true positives, true negatives, false positives and false negatives of class  $c$ , respectively.  $N$  is the total number of pixels in all classes including the background.

#### 4.1.3 Implementation Details

All models in the experiments were implemented with PyTorch framework on a single NVIDIA GTX 2080ti GPU with batch size of 4. For fast convergence, we deployed the AdamW optimizer to train all models in the experiments (Loshchilov and Hutter, 2017). The base learning rate was set to  $1e-4$  and the weight decay value was 0.01. The early stopping technique was applied to control the training time and to prevent overfitting. Cross-entropy loss was chosen as the loss function. Only scale-invariant image transformation (random flip) was used for data augmentation.

#### 4.1.4 Comparative benchmark methods

To test the cross-resolution generalization capability of the proposed SaNet, we selected various benchmark methods for semantic segmentation of MSR aerial images for comparison, including multi-scale feature aggregation models like the feature pyramid network (FPN) (Lin et al., 2017) and pyramid scene network (PSPNet) (Zhao et al., 2017), and the multi-view context aggregation method Deeplabv3+ (Chen et al., 2018a), as well as state-of-the-art models proposed for remotely sensed semantic labelling, such as the dense dilated convolutions merging network (DDCM-Net) (Liu et al., 2020) and edge-aware neural network (EaNet) (Zheng et al., 2020). Besides, ablation studies were conducted with the following model design: (1) An upsampling operation was employed on top of the backbone to construct the single-scale network Baseline. The feature maps produced by the Baseline were restored directly to the same size as the original input image. (2) The spatial relationship module (SRM) (Mou et al., 2020) and our SFR were added into the Baseline

to construct two spatial relationship networks (i.e., Baseline+SRM and Baseline+SFR). (3) The FPN module (Lin et al., 2017) and our DCFPN were embedded into the Baseline to construct two multi-scale networks (i.e., Baseline+FPN and Baseline+DCFPN).

## 4.2 Experimental results on resampled MSR aerial images

Due to the limitation of GPU memory, the raw TOP image tiles of the Vaihingen and Potsdam datasets were cropped into  $512 \times 512$  pixel patches. We applied a resize operation before cropping to generate the test sets, to assess the performance of SaNet on resampled MSR aerial images. Specifically, we first resampled the image tiles of the original Vaihingen test set into 0.75 times and then cropped them into  $512 \times 512$  pixel patches, to generate the  $0.75 \times$  Vaihingen test set. The  $0.5 \times$  and  $0.25 \times$  Vaihingen test sets were produced in the same fashion. We created four Potsdam test sets with different spatial resolutions using the same strategy. Data details are listed in **Table 1**.

**TABLE 1.** Details of the four Vaihingen test sets and the four Potsdam test sets.

Dataset	Spatial Resolution (cm)	Patch Size (pixels)	Patch Numbers
<b>Vaihingen test sets</b>			
Original	9	$512 \times 512$	398
$0.75 \times$	12	$512 \times 512$	230
$0.5 \times$	18	$512 \times 512$	113
$0.25 \times$	36	$512 \times 512$	38
<b>Potsdam test sets</b>			
Original	5	$512 \times 512$	2016
$0.75 \times$	6.67	$512 \times 512$	1134
$0.5 \times$	10	$512 \times 512$	504
$0.25 \times$	20	$512 \times 512$	126

### 4.2.1 Ablation study on resampled aerial images

To evaluate the performance of the SFR and DCFPN modules separately in the semantic mapping of MSR aerial images, we chose ResNet101 as the backbone (He et al., 2016) and conducted ablation experiments on the four Vaihingen test sets in **TABLE 1**.

*Ablation study for densely connected feature pyramid network module:* As listed in **TABLE 2**, compared to the Baseline, the utilization of FPN and DCFPN produced a significant increase in the mean OA (3.4% and 4.0%), which demonstrates the validity of multi-scale representation and the superiority of our DCFPN in comparison with FPN.

*Ablation study for the spatial feature recalibration module:* With the application of SRM and SFR, the mean OA increased by 3.9% and 5.0%, respectively, compared to Baseline (**TABLE 2**). Particularly, Baseline+SFR outperforms Baseline by 10.2% and exceeds Baseline+SRM by 2.8% on the  $0.25 \times$  Vaihingen test set. These results suggest that enhancing information on the global spatial relationship could strengthen the adaptability of the network to MSR aerial images. The significant increase in accuracy demonstrates the advantage of our SFR in modelling spatial relationships. Moreover, by combining DCFPN and SFR, our SaNet maintains the highest OA on the four Vaihingen test sets (**TABLE 2**).

**TABLE 2.** Ablation Study for the SFR module and DCFPN module. The backbone is ResNet101. Original,  $0.75 \times$ ,  $0.5 \times$  and  $0.25 \times$  represent the four Vaihingen test sets.

Method	OA				Mean OA
	original	$0.75 \times$	$0.5 \times$	$0.25 \times$	
Baseline	88.3	82.9	76.2	59.6	76.8
FPN (Baseline+FPN) (Lin et al., 2017)	89.6	85.5	80.3	65.2	80.2
Baseline+DCFPN	89.8	86.0	81.0	66.2	80.8
Baseline+SRM (Mou et al., 2020)	89.7	85.6	80.6	67.0	80.7
Baseline+SFR	90.2	85.9	81.3	69.8	81.8
SaNet (Baseline+SFR+DCFPN)	<b>91.0</b>	<b>87.1</b>	<b>83.1</b>	<b>72.5</b>	<b>83.4</b>

### 4.2.2 Comparison with state-of-the-art models on the four Vaihingen test sets

To further test the proposed SaNet for cross-resolution segmentation, we chose ResNet101 (He et al., 2016) as the backbone network and compared SaNet with other state-of-the-art methods on the four Vaihingen test sets. The Baseline+SRM was also selected



for comparison as a competitive spatial relationship network. Experimental results demonstrate that the proposed SaNet outperforms other models in both mean F1 score (77.4%) and OA (83.4%) (TABLE 3). Specifically, SaNet increased the average OA by 6.6%, 2.7% and 2.6% in comparison with Baseline, Baseline+SRM and Deeplabv3+, respectively. Moreover, SaNet produced increments of 2.4% and 2.0% in the F1 score compared with the state-of-the-art methods DDCM-Net and EaNet. Especially, SaNet is superior in both OA and F1 score on the  $0.25\times$  Vaihingen test set.

With decreased spatial resolution, Baseline with single-scale representation declines at the fastest rate, as shown in Fig. 2 (a), followed by the multi-scale representation networks FPN, PSPNet, and Deeplabv3+ as well as the spatial relationship network Baseline+SRM and the state-of-the-art networks DDCM-Net and EaNet. In contrast, the accuracy of SaNet reduces at the slowest rate. The OA secants (dashed lines) in Fig. 2 (b) represent the declining magnitude of the OA when the spatial resolution decreases from the original to  $0.25\times$ . The proposed SaNet produces the smallest rate of decline.

As shown in Fig. 3, the proposed SaNet achieved the most accurate segmentation maps compared with other methods. Particularly, the semantic content of geospatial objects (e.g. impervious surface) is characterized effectively (Fig. 3). Meanwhile, the complex contour of buildings is preserved completely in the  $0.25\times$  Vaihingen test set.

TABLE 3. Quantitative comparison with state-of-the-art models on the four Vaihingen test sets. The backbone is ResNet101. The values in bold are the best.

Method	F1-score				OA				Mean F1-score	Mean OA
	original	$0.75\times$	$0.5\times$	$0.25\times$	original	$0.75\times$	$0.5\times$	$0.25\times$		
Baseline	84.9	76.4	65.9	48.2	88.3	82.9	76.2	59.6	68.9	76.8
Baseline+SRM (Mou et al., 2020)	87.7	80.6	70.3	53.6	89.7	85.6	80.6	67.0	73.1	80.7
FPN (Lin et al., 2017)	88.0	81.7	72.1	53.3	89.6	85.5	80.3	65.2	73.8	80.2
PSPNet (Zhao et al., 2017)	87.0	79.8	69.9	52.3	89.6	85.2	79.6	64.8	72.3	79.8
Deeplabv3+ (Chen et al., 2018a)	88.7	81.8	72.5	54.0	90.1	85.8	80.9	66.5	74.3	80.8
DDCM-Net (Liu et al., 2020)	89.6	82.0	72.4	55.9	90.6	86.0	81.4	68.6	75.0	81.7
EaNet (Zheng et al., 2020)	89.8	82.6	73.4	55.9	90.7	86.1	81.2	68.0	75.4	81.5
SaNet (ours)	<b>90.3</b>	<b>84.3</b>	<b>75.9</b>	<b>59.2</b>	<b>91.0</b>	<b>87.1</b>	<b>83.1</b>	<b>72.5</b>	<b>77.4</b>	<b>83.4</b>

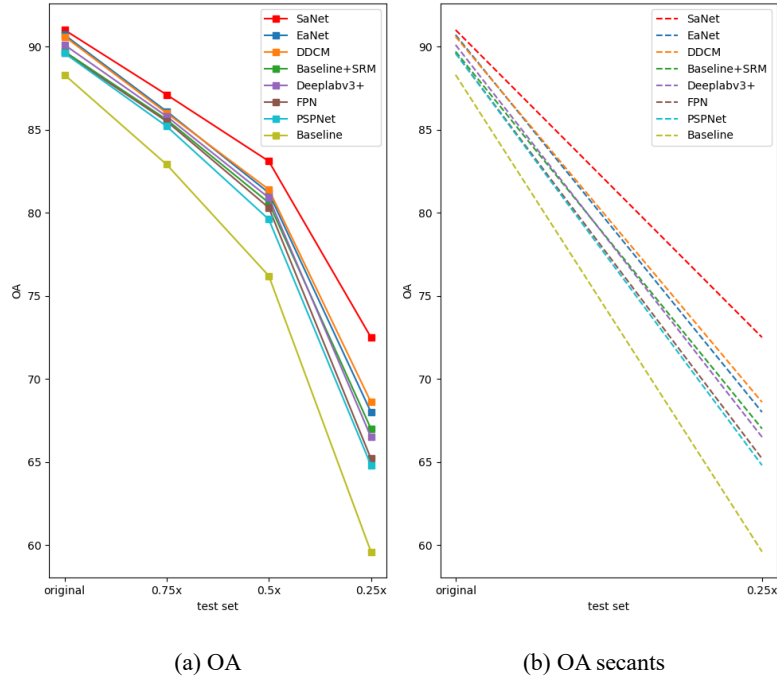
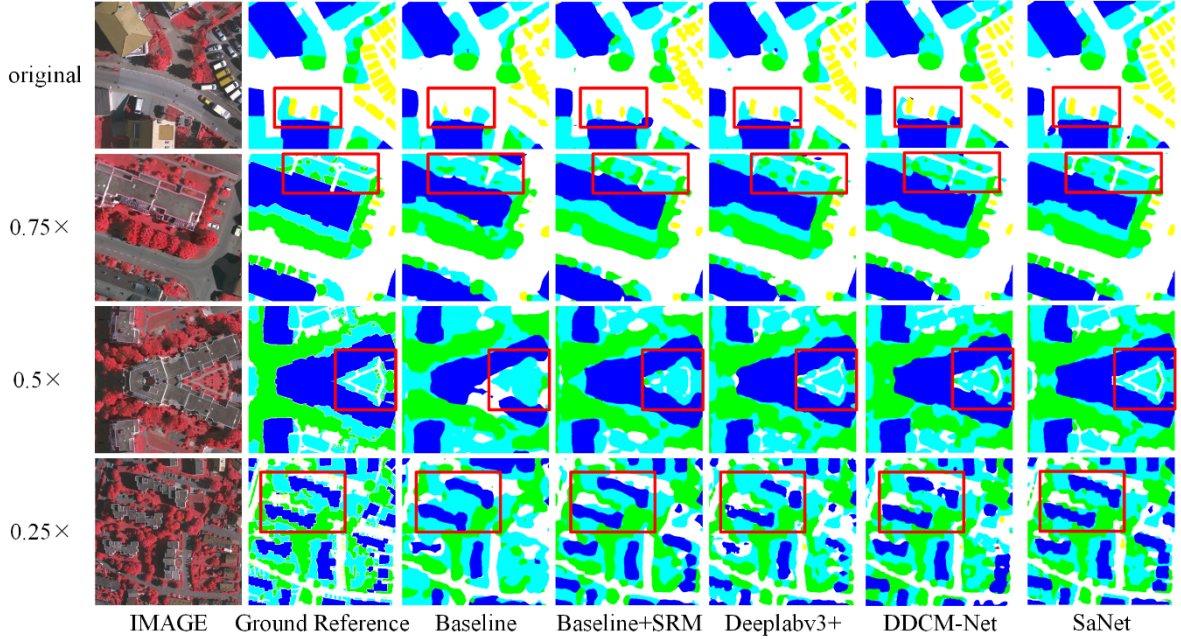


Fig. 2 (a) OA vs. the four Vaihingen test sets. (b) Secants of the OA vs. the two Vaihingen test sets, indicating the declining magnitude when spatial resolution decreases from the original to  $0.25\times$ .





**Fig. 3** Visual comparison between our SaNet and other state-of-the-art models applied to the four Vaihing test sets. Each image is a  $512 \times 512$  pixel patch. The enlarged regions are marked by red boxes. Legend: impervious surface: white, building: blue, low vegetation: cyan, tree: green, car: yellow, clutter: red.

#### 4.2.3 Comparison with state-of-the-art models on the four Potsdam test sets

The Potsdam dataset is larger than the Vaihing dataset and more complex in terms of spatial details. We carried out comprehensive experiments on the four Potsdam test sets in **TABLE 1** to test the generalization capability of SaNet. Despite the intricate details in the images, our SaNet maintains superiority in both the mean F1 score (80.4%) and mean OA (83.4%) (**TABLE 4**). Particularly, SaNet exceeds all multi-scale contextual information aggregation methods, including Deeplabv3+, DDCM-Net and EaNet, by 3.3%, 2.3% and 2.2% in mean OA. For the  $0.25 \times$  Potsdam test set, our SaNet delivers a respectable OA (69.7%) and F1 score (58.4%), outperforming the sub-optimal model by a large margin of 3.0% in the F1 score. The above-mentioned accuracy demonstrates the effectiveness and robustness of our SaNet for the cross-resolution segmentation of aerial images. Moreover, SaNet yields the smallest declining magnitude (**Fig. 4 (a)**) and achieves the most gentle rate of decline in accuracy with coarsening spatial resolution (**Fig. 4 (b)**).

**TABLE 4:** Quantitative comparison of SaNet with state-of-the-art models applied to the four Potsdam test sets. The backbone is ResNet101. The values in bold are the best.

Method	F1-score				OA				Mean F1-score	Mean OA
	original	$0.75 \times$	$0.5 \times$	$0.25 \times$	original	$0.75 \times$	$0.5 \times$	$0.25 \times$		
Baseline	87.8	82.1	73.5	47.9	86.9	83.5	77.9	58.3	72.8	76.7
Baseline+SRM (Mou et al., 2020)	90.4	85.4	76.8	55.0	89.2	86.4	81.5	65.6	76.9	80.7
FPN (Lin et al., 2017)	90.4	85.9	78.0	52.1	88.9	86.2	81.4	63.9	76.6	80.1
PSPNet (Zhao et al., 2017)	90.5	85.2	76.1	52.8	89.5	86.3	80.8	62.0	76.2	79.7
Deeplabv3+ (Chen et al., 2018a)	90.0	85.4	77.8	51.3	88.8	86.1	81.3	64.0	76.1	80.1
DDCM-Net (Liu et al., 2020)	91.7	87.3	76.4	55.0	90.1	87.2	82.4	64.5	77.6	81.1
EaNet (Zheng et al., 2020)	91.9	87.1	78.8	55.4	90.4	87.2	82.3	65.0	78.3	81.2
SaNet (ours)	<b>92.3</b>	<b>88.3</b>	<b>82.4</b>	<b>58.4</b>	<b>90.9</b>	<b>88.4</b>	<b>84.7</b>	<b>69.7</b>	<b>80.4</b>	<b>83.4</b>

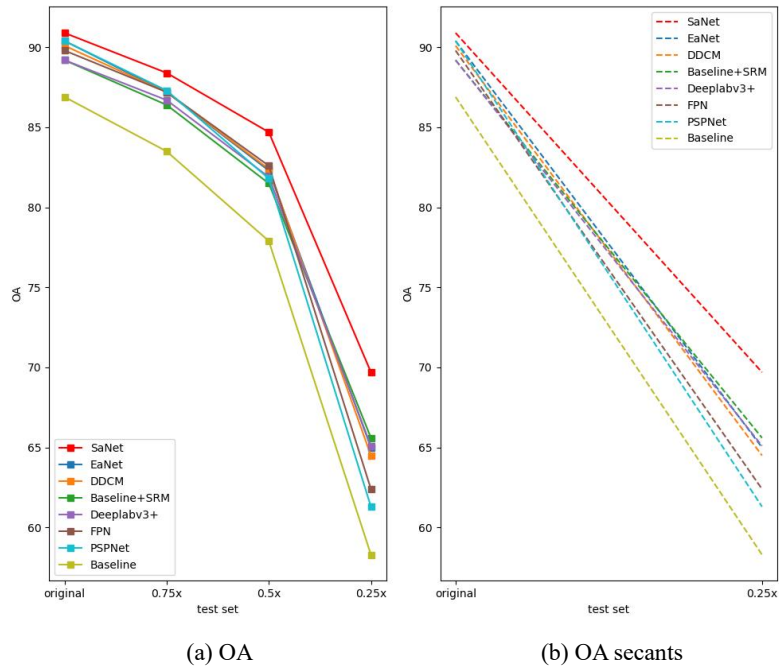


**Fig. 4** (a) OA vs. the four Potsdam test sets. (b) Secants of the OA vs. the two Potsdam test sets, denoting the declining magnitude when spatial resolution decreases from the original to  $0.25\times$ .

The segmentation results are shown in **Fig. 5**, where regions with obvious improvement are marked by red boxes. The proposed SaNet with DCFPN and SFR exhibits the smoothest visual appearance with the least red clutter noise, as shown in the first row of **Fig. 5**. Labelling buildings with scale-aware features extracted by SaNet is more capable of recreating the complete object. For example, SaNet recognizes the complete, regular shape of the main building as shown in the second row of **Fig. 5**, where other methods draw out the building into an incomplete and irregular semantic object due to the interference of impervious surface. In the  $0.25\times$  image, the SaNet represents the geometries of two adjacent buildings in the red box region effectively, whereas other approaches identify them as a single object (fourth row of **Fig. 5**). Meanwhile, small objects like cars are also identified accurately in the third row of **Fig. 5**.

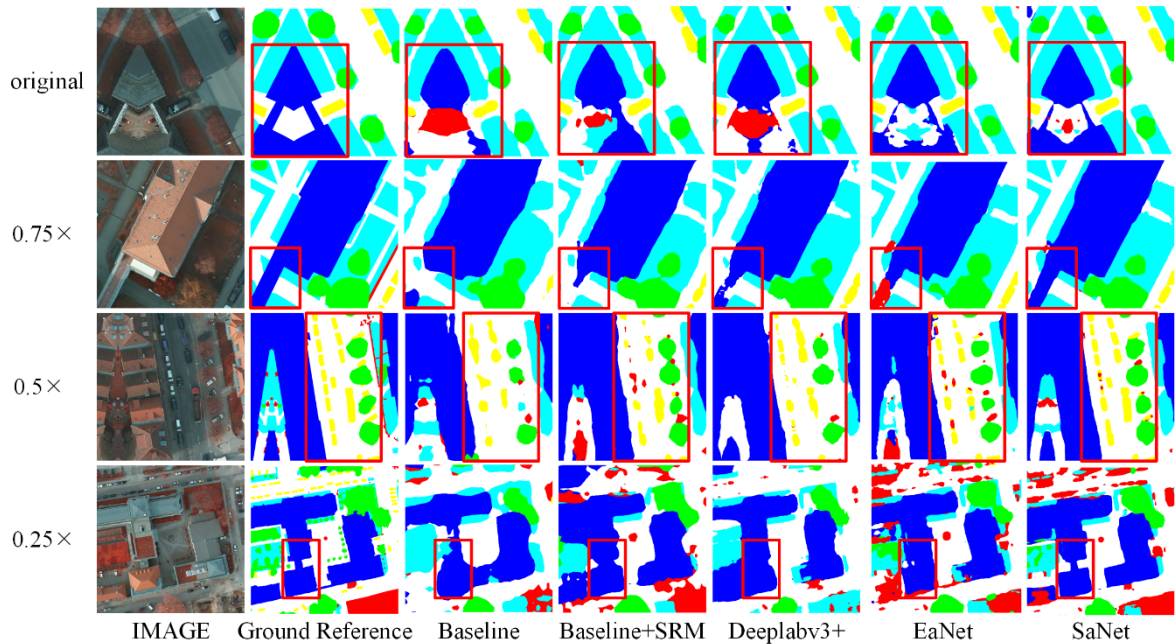


**Fig. 5** Visual comparison between our SaNet and other state-of-the-art models applied to the four Potsdam test sets. Each image is a  $512\times 512$  pixel patch. Legend: impervious surface: white, building: blue, low vegetation: cyan, tree: green, car: yellow, clutter: red.

### 4.3 Experimental results on the raw MSR aerial images

The Vaihingen and Potsdam datasets include the same categories (impervious surface, building, low vegetation, tree, car, and clutter) and multispectral bands (Near Infrared, Red, Green), but with different spatial resolutions (GSD of 9 cm and 5 cm, respectively). Hence, training on the Potsdam dataset, but testing on the Vaihingen dataset is a useful way to investigate the cross-resolution segmentation performance of the network on raw aerial images. Specifically, in this experiment, we trained the networks on the original Potsdam training set and tested the performance on the original Vaihingen test set. The other experimental settings are identical to 4.1.3.

#### 4.3.1 Ablation study on raw MSR aerial images

We conducted additional ablation experiments to demonstrate the validity and superiority of SFR and DCFPN on raw aerial images at diverse spatial resolutions. As illustrated in TABLE 5, the deployment of FPN and DCFPN produced significant increases of 5.4% and 12.7% in the average F1 score compared to the Baseline, demonstrating the effectiveness of multi-scale representation for semantic labelling of MSR aerial images as well as the advantage of DCFPN.

Moreover, Baseline+SFR outperformed Baseline by 16.1% in the mean F1 score, which further indicates that modelling spatial relationships could enhance feature representation of MSR aerial images. Meanwhile, the per-class F1 score of Baseline+SFR exceeded that of Baseline+SRM, showing the superiority of our SFR.

The proposed SaNet maintained the highest F1-score in all categories, thanks to the simultaneous employment of SFR and DFPN. Especially, SaNet obtained a balanced performance between large objects (e.g. Tree) and small objects (e.g. Car), which demonstrates the ability to pay equal attention to objects of different sizes.

TABLE 5. Ablation Study for the SFR module and DCFPN module. The backbone is ResNet101. The values in bold are the best.

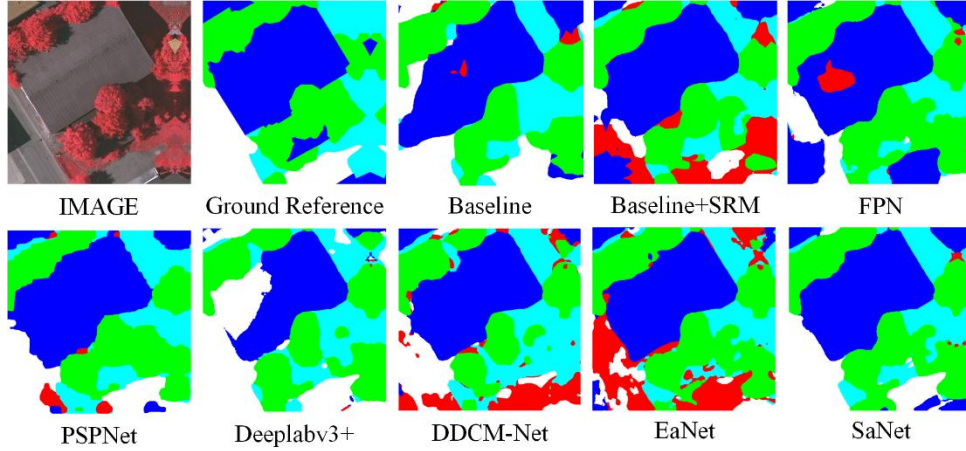
Method	F1-score					Mean
	Imp Surf	Building	Low veg	Tree	Car	F1-score
Baseline	50.3	64.4	34.2	72.7	16.0	47.5
FPN (Baseline+FPN) (Lin et al., 2017)	44.2	76.5	42.1	74.5	27.3	52.9
Baseline+DCFPN	58.9	78.8	47.6	74.8	40.9	60.2
Baseline+SRM (Mou et al., 2020)	63.0	74.3	43.4	68.2	39.3	57.6
Baseline+SFR	66.6	79.0	44.5	72.0	45.3	61.5
SaNet (Baseline+SFR+DCFPN)	<b>70.4</b>	<b>84.5</b>	<b>48.4</b>	<b>77.2</b>	<b>56.5</b>	<b>67.4</b>

#### 4.3.2 Comparison with state-of-the-art models

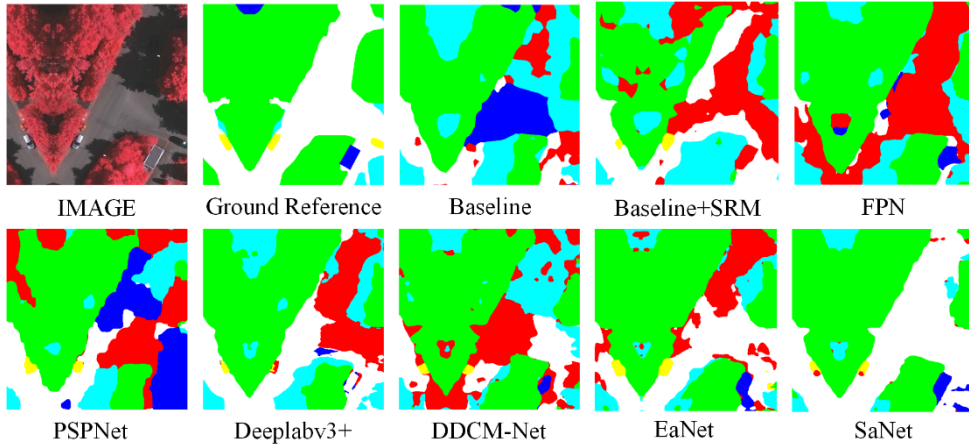
Classification accuracy is compared in TABLE 6. Generally, the obtained accuracy is relatively low compared to the previous experiments. The major reason is that variation exists between the Vaihingen and Potsdam datasets. Even with this variation in image characteristics, the proposed SaNet achieved the top prediction scores in terms of average F1 (67.4%) and OA (65.9%). Notably, our SaNet is at least 7.4% and 15.5% higher than other methods for the impervious surface and car classes. The numerical results demonstrate the greater generalization capability of our SaNet in cross-resolution segmentation compared with other state-of-the-art methods. As shown in Figs. 6 and 7. The proposed SaNet segmented the building with accurate and complete boundaries, whereas other benchmark approaches depict a coarse-structured building. Meanwhile, other benchmarks misclassified impervious surfaces as clutter due to the interference of shadow. In contrast, our SaNet distinguished impervious surfaces accurately.

TABLE 6. Quantitative comparison of SaNet with state-of-the-art models. The backbone is ResNet101. The best values are in bold.

Method	F1-score					Mean	OA
	Imp Surf	Building	Low veg	Tree	Car	F1-score	
Baseline	50.3	64.4	34.2	72.7	16.0	47.5	53.1
Baseline+SRM (Mou et al., 2020)	63.0	74.3	43.4	68.2	39.3	57.6	56.9
FPN (Lin et al., 2017)	44.2	76.5	42.1	74.5	27.3	52.9	56.4
PSPNet (Zhao et al., 2017)	54.5	79.3	41.3	72.3	40.8	57.6	56.2
Deeplabv3+ (Chen et al., 2018a)	52.1	76.3	39.9	74.5	28.1	54.2	58.7
DDCM-Net (Liu et al., 2020)	61.5	81.3	46.9	77.8	28.3	59.2	61.8
EaNet (Zheng et al., 2020)	57.5	80.8	44.2	77.5	41.0	60.2	61.1
SaNet (Ours)	<b>70.4</b>	<b>84.5</b>	<b>48.5</b>	<b>77.2</b>	<b>56.5</b>	<b>67.4</b>	<b>65.9</b>



**Fig.6** Visual comparisons between our SaNet and other state-of-the-art models. The image size is  $512 \times 512$ . Legend: impervious surface: white, building: blue, low vegetation: cyan, tree: green, car: yellow, clutter: red.



**Fig. 7** Visual comparisons between our SaNet and other state-of-the-art models. The image size is  $512 \times 512$ . Legend: impervious surface: white, building: blue, low vegetation: cyan, tree: green, car: yellow, clutter: red.

#### 4.4 Discussion

The comprehensive experiments demonstrate the superiority of our SaNet for cross-resolution segmentation of aerial images. Three vital factors enable the proposed SaNet to produce competitive accuracies. First, the proposed SFR module models the invariant global spatial relationships to alleviate the contradiction between complete feature extraction and information loss at coarse spatial resolutions. Conventionally, the single-branched structure is used frequently to capture the global spatial relationships of networks, but this shows weak adaptability to MSR aerial images due to the fixed size of the branching feature. By contrast, our SFR employs a dual-branched structure, where the global spatial relationships are modelled at different scales to tackle cross-resolution segmentation. Second, the proposed DCFPN resolves the imbalanced segmentation quality of large and small objects. The traditional FPN fuses the high-level semantic features and low-level detailed features to capture multi-scale contexts. Although this can ease the negative impact brought about by the scale variation of ground objects, the limited receptive field of extracted features severely restricts its representation capability in MSR aerial images. Nevertheless, our DCFPN creates three large field connections to enrich the receptive field of semantic features, providing high-quality multi-scale contextual information. Besides, instead of fusing features directly, our DCFPN employs a weighting operation to aggregate multi-layer and multi-view features, ensuring the robustness of the fused features. Third, building on the advantages of SFR and DCFPN, our SaNet can capture scale-aware contexts for robust semantic segmentation of MSR aerial images.

The smoothest segmentation maps generated by our SaNet demonstrate the ability to capture large objects (e.g. buildings) with complete and fine geometries and pay equal attention to small objects (e.g. cars) simultaneously. However, the extra computational burden caused by DCFPN and SFR reduced the computational efficiency of our SaNet. In future research, we will design a more efficient deep network to learn scale-aware features for semantic labelling of MSR aerial images.

## 5. CONCLUSION

Cross-resolution aerial image segmentation is a challenging task due to the large-scale variation and informative feature loss in MSR aerial images. In this paper, we present a scale-aware neural network (SaNet) with two novel modules for robust segmentation

of MSR aerial images, including spatial feature recalibration (SFR) and a densely connected feature pyramid network (DCFPN). We found that both multi-scale representation and spatial relationship enhancement increased the adaptability of the network to MSR aerial images. The proposed SFR module was superior in characterising the spatial relationships of the network compared to the SRM module, while the proposed DCFPN module captured high-quality multi-scale semantic information from MSR aerial images by merging various features. The combination of DCFPN and SFR in SaNet increased classification accuracy further.

Our SaNet demonstrated strong cross-resolution generalization ability compared with other models, including the spatial relationship model (Baseline+SRM) and specially designed multi-scale models (FPN, PSPNet, and Deeplabv3+), as well as state-of-the-art models (DDCM-Net and EaNet). Moreover, the SaNet maintained outstanding accuracy on raw MSR aerial images, even though subject to variation between training and testing datasets.

## ACKNOWLEDGEMENT

This research was funded by National Natural Science Foundation of China (NSFC) under grant number 41971352, National Key Research and Development Program of China under grant number 2018YFB0505003. The authors are very grateful to the many people who helped to comment on the article, and the Large Scale Environment Remote Sensing Platform (Facility No. 16000009, 16000011, 16000012) provided by Wuhan University. Special thanks to editors and reviewers for providing valuable insight into this article.

## REFERENCES

- Atkinson, P.M., Tate, N.J., 2000. Spatial Scale Problems and Geostatistical Solutions: A Review. *The Professional Geographer* 52, 607-623.
- Audebert, N., Le Saux, B., Lefèvre, S., 2018. Beyond RGB: Very high resolution urban remote sensing with multimodal deep networks. *ISPRS Journal of Photogrammetry and Remote Sensing* 140, 20-32.
- Bell, S., Zitnick, C.L., Bala, K., Girshick, R., 2016. Inside-outside net: Detecting objects in context with skip pooling and recurrent neural networks, Proceedings of the IEEE/CVF Conference on Computer Vision and Pattern Recognition, pp. 2874-2883.
- Cai, Z., Fan, Q., Feris, R.S., Vasconcelos, N., 2016. A Unified Multi-scale Deep Convolutional Neural Network for Fast Object Detection, in: Leibe, B., Matas, J., Sebe, N., Welling, M. (Eds.), Proceedings of the European conference on computer vision (ECCV). Springer International Publishing, Cham, pp. 354-370.
- Chen, L.-C., Papandreou, G., Schroff, F., Adam, H., 2017. Rethinking atrous convolution for semantic image segmentation. arXiv preprint arXiv:1706.05587.
- Chen, L.-C., Yang, Y., Wang, J., Xu, W., Yuille, A.L., 2016. Attention to scale: Scale-aware semantic image segmentation, Proceedings of the IEEE/CVF Conference on Computer Vision and Pattern Recognition, pp. 3640-3649.
- Chen, L.-C., Zhu, Y., Papandreou, G., Schroff, F., Adam, H., 2018a. Encoder-decoder with atrous separable convolution for semantic image segmentation, Proceedings of the European conference on computer vision (ECCV), pp. 801-818.
- Chen, L., Papandreou, G., Kokkinos, I., Murphy, K., Yuille, A.L., 2018b. DeepLab: Semantic Image Segmentation with Deep Convolutional Nets, Atrous Convolution, and Fully Connected CRFs. *IEEE Transactions on Pattern Analysis and Machine Intelligence* 40, 834-848.
- Cheng, X., Wang, P., Yang, R., 2018. Depth estimation via affinity learned with convolutional spatial propagation network, Proceedings of the European conference on computer vision (ECCV), pp. 103-119.
- Fu, J., Liu, J., Tian, H., Li, Y., Bao, Y., Fang, Z., Lu, H., 2019. Dual attention network for scene segmentation, Proceedings of the IEEE/CVF Conference on Computer Vision and Pattern Recognition, pp. 3146-3154.
- Ge, Y., Jin, Y., Stein, A., Chen, Y., Wang, J., Wang, J., Cheng, Q., Bai, H., Liu, M., Atkinson, P.M., 2019. Principles and methods of scaling geospatial Earth science data. *Earth-Science Reviews* 197, 102897.
- Ghiasi, G., Lin, T.-Y., Le, Q.V., 2019. Nas-fpn: Learning scalable feature pyramid architecture for object detection, Proceedings of the IEEE/CVF Conference on Computer Vision and Pattern Recognition, pp. 7036-7045.
- Griffiths, D., Boehm, J., 2019. Improving public data for building segmentation from Convolutional Neural Networks (CNNs) for fused airborne lidar and image data using active contours. *ISPRS Journal of Photogrammetry and Remote Sensing* 154, 70-83.
- Guo, Y., Jia, X., Paull, D., 2018. Effective Sequential Classifier Training for SVM-Based Multitemporal Remote Sensing Image Classification. *IEEE Transactions on Image Processing* 27, 3036-3048.
- He, K., Zhang, X., Ren, S., Sun, J., 2016. Deep residual learning for image recognition, Proceedings of the IEEE/CVF Conference on Computer Vision and Pattern Recognition, pp. 770-778.
- Hu, H., Gu, J., Zhang, Z., Dai, J., Wei, Y., 2019. Relation networks for object detection, Proceedings of the IEEE/CVF Conference on Computer Vision and Pattern Recognition, pp. 3588-3597.
- Huang, S., Liu, S., Hui, T., Han, J., Li, B., Feng, J., Yan, S., 2020. ORDNet: Capturing Omni-Range Dependencies for Scene Parsing. *IEEE Transactions on Image Processing* 29, 8251-8263.
- Jaderberg, M., Simonyan, K., Zisserman, A., Kavukcuoglu, K., 2015. Spatial transformer networks. arXiv preprint arXiv:1506.02025.
- Kaiser, P., Wegner, J.D., Lucchi, A., Jaggi, M., Hofmann, T., Schindler, K., 2017. Learning Aerial Image Segmentation From Online Maps. *IEEE Transactions on Geoscience and Remote Sensing* 55, 6054-6068.
- Li, R., Duan, C., Zheng, S., Zhang, C., Atkinson, P.M., 2021a. MACU-Net for Semantic Segmentation of Fine-Resolution Remotely Sensed Images. *IEEE Geoscience and Remote Sensing Letters* 10.1109/LGRS.2021.3052886.
- Li, R., Li, K., Kuo, Y.-C., Shu, M., Qi, X., Shen, X., Jia, J., 2018. Referring image segmentation via recurrent refinement networks, Proceedings of the IEEE Conference on Computer Vision and Pattern Recognition, pp. 5745-5753.
- Li, R., Zheng, S., Duan, C., Su, J., Ce, Z., 2021b. Multistage Attention ResU-Net for Semantic Segmentation of Fine-Resolution Remote Sensing Images. *IEEE Geoscience and Remote Sensing Letters*.
- Lin, T.-Y., Dollár, P., Girshick, R., He, K., Hariharan, B., Belongie, S., 2017. Feature pyramid networks for object detection, Proceedings of the IEEE/CVF Conference on Computer Vision and Pattern Recognition, pp. 2117-2125.

- Liu, Q., Kampffmeyer, M., Jenssen, R., Salberg, A.B., 2020. Dense Dilated Convolutions' Merging Network for Land Cover Classification. *IEEE Transactions on Geoscience and Remote Sensing* 58, 6309-6320.
- Liu, S., De Mello, S., Gu, J., Zhong, G., Yang, M.-H., Kautz, J., 2017. Learning affinity via spatial propagation networks. *arXiv preprint arXiv:1710.01020*.
- Liu, S., Qi, L., Qin, H., Shi, J., Jia, J., Path aggregation network for instance segmentation, *Proceedings of the IEEE/CVF Conference on Computer Vision and Pattern Recognition*, pp. 8759-8768.
- Long, J., Shelhamer, E., Darrell, T., 2015. Fully convolutional networks for semantic segmentation, *Proceedings of the IEEE/CVF Conference on Computer Vision and Pattern Recognition*, pp. 3431-3440.
- Loshchilov, I., Hutter, F., 2017. Decoupled weight decay regularization. *arXiv preprint arXiv:1711.05101*.
- Mou, L., Hua, Y., Zhu, X.X., 2020. Relation Matters: Relational Context-Aware Fully Convolutional Network for Semantic Segmentation of High-Resolution Aerial Images. *IEEE Transactions on Geoscience and Remote Sensing* 58, 7557-7569.
- Pal, M., 2005. Random forest classifier for remote sensing classification. *International Journal of Remote Sensing* 26, 217-222.
- Pan, X., Shi, J., Luo, P., Wang, X., Tang, X., 2018. Spatial as deep: Spatial cnn for traffic scene understanding, *Proceedings of the AAAI Conference on Artificial Intelligence*, 1 ed.
- Persello, C., Stein, A., 2017. Deep Fully Convolutional Networks for the Detection of Informal Settlements in VHR Images. *IEEE Geoscience and Remote Sensing Letters* 14, 2325-2329.
- Roy, S.K., Krishna, G., Dubey, S.R., Chaudhuri, B.B.J.I.G., Letters, R.S., 2019. HybridSN: Exploring 3-D-2-D CNN feature hierarchy for hyperspectral image classification. *17*, 277-281.
- Santoro, A., Raposo, D., Barrett, D.G.T., Malinowski, M., Pascanu, R., Battaglia, P., Lillicrap, T., 2017. A simple neural network module for relational reasoning. *arXiv preprint arXiv:1706.01427*.
- Singh, B., Davis, L.S., 2018. An Analysis of Scale Invariance in Object Detection - SNIP, 2018 *IEEE/CVF Conference on Computer Vision and Pattern Recognition*, pp. 3578-3587.
- Tan, M., Pang, R., Le, Q.V., 2020. Efficientdet: Scalable and efficient object detection, *Proceedings of the IEEE/CVF conference on computer vision and pattern recognition*, pp. 10781-10790.
- Wang, X., Girshick, R., Gupta, A., He, K., 2018. Non-local neural networks, *Proceedings of the IEEE conference on computer vision and pattern recognition*, pp. 7794-7803.
- Wei, Y., Wang, Z., Xu, M., 2017. Road Structure Refined CNN for Road Extraction in Aerial Image. *IEEE Geoscience and Remote Sensing Letters* 14, 709-713.
- Xu, J., Cao, Y., Zhang, Z., Hu, H., 2019. Spatial-temporal relation networks for multi-object tracking, *Proceedings of the IEEE/CVF International Conference on Computer Vision*, pp. 3988-3998.
- Zhang, C., Harrison, P.A., Pan, X., Li, H., Sargent, I., Atkinson, P.M., 2020. Scale Sequence Joint Deep Learning (SS-JDL) for land use and land cover classification. *Remote Sensing of Environment* 237, 111593.
- Zhang, C., Pan, X., Li, H., Gardiner, A., Sargent, I., Hare, J., Atkinson, P.M., 2018a. A hybrid MLP-CNN classifier for very fine resolution remotely sensed image classification. *ISPRS Journal of Photogrammetry and Remote Sensing* 140, 133-144.
- Zhang, C., Sargent, I., Pan, X., Li, H., Gardiner, A., Hare, J., Atkinson, P.M., 2018b. An object-based convolutional neural network (OCNN) for urban land use classification. *Remote Sensing of Environment* 216, 57-70.
- Zhang, C., Sargent, I., Pan, X., Li, H., Gardiner, A., Hare, J., Atkinson, P.M., 2019. Joint Deep Learning for land cover and land use classification. *Remote Sensing of Environment* 221, 173-187.
- Zhao, H., Qi, X., Shen, X., Shi, J., Jia, J., 2018a. Icnets for real-time semantic segmentation on high-resolution images, *Proceedings of the European conference on computer vision (ECCV)*, pp. 405-420.
- Zhao, H., Shi, J., Qi, X., Wang, X., Jia, J., 2017. Pyramid scene parsing network, *Proceedings of the IEEE conference on computer vision and pattern recognition*, pp. 2881-2890.
- Zhao, H., Zhang, Y., Liu, S., Shi, J., Loy, C.C., Lin, D., Jia, J., 2018b. Psanet: Point-wise spatial attention network for scene parsing, *Proceedings of the European Conference on Computer Vision (ECCV)*, pp. 267-283.
- Zhao, W., Du, S., 2016. Learning multiscale and deep representations for classifying remotely sensed imagery. *ISPRS Journal of Photogrammetry and Remote Sensing* 113, 155-165.
- Zheng, X., Huan, L., Xia, G.-S., Gong, J., 2020a. Parsing very high resolution urban scene images by learning deep ConvNets with edge-aware loss. *ISPRS Journal of Photogrammetry and Remote Sensing* 170, 15-28.
- Zheng, Z., Zhong, Y., Ma, A., Han, X., Zhao, J., Liu, Y., Zhang, L., 2020b. HyNet: Hyper-scale object detection network framework for multiple spatial resolution remote sensing imagery. *ISPRS Journal of Photogrammetry and Remote Sensing* 166, 1-14.
- Zhong, P., Wang, R., 2007. A Multiple Conditional Random Fields Ensemble Model for Urban Area Detection in Remote Sensing Optical Images. *IEEE Transactions on Geoscience and Remote Sensing* 45, 3978-3988.